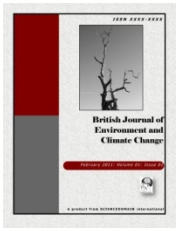

British Journal of Environment & Climate Change
3(4): 566-586, 2013

SCIENCEDOMAIN *international*
www.sciencedomain.org

Combining Active and Passive Airborne Remote Sensing to Quantify NO_2 and O_x Production near Bakersfield, CA

Sunil Baidar[1,2], Rainer Volkamer[1,2,*], Raul Alvarez[3], Alan Brewer[3], Fay Davies[4], Andy Langford[3], Hilke Oetjen[1], Guy Pearson[5], Christoph Senff[2,3] and R. Michael Hardesty[2,3]

[1]Department of Chemistry and Biochemistry, University of Colorado, Boulder, CO, USA.
[2]Cooperative Institute for Research in Environmental Sciences, Boulder, CO, USA.
[3]Earth System Research Laboratory, NOAA, Boulder, CO, USA.
[4]School of Built Environment, University of Salford, Salford, UK.
[5]Halo Photonics, Worcestershire, UK.

Authors' contributions

Authors RV, CS and RMH designed research; all authors performed research. Authors SB, HO, AB and CS analyzed data; authors SB and RV interpreted data and wrote the paper. All authors provided comments.

Original Research Article

Received 1st July 2013
Accepted 23rd September 2013
Published 18th November 2013

ABSTRACT

Aims: The objective of this study is to demonstrate the integrated use of passive and active remote sensing instruments to quantify the rate of NO_x emissions, and investigate the O_x production rates from an urban area.
Place and Duration of Study: A research flight on June 15, 2010 was conducted over Bakersfield, CA and nearby areas with oil and natural gas production.
Methodology: Three remote sensing instruments, namely the University of Colorado AMAX-DOAS, NOAA TOPAZ lidar, and NCAS Doppler lidar were deployed aboard the NOAA Twin Otter during summer 2010. Production rates of nitrogen dioxide (NO_2) and O_x' (background corrected O_3 + NO_2) were quantified using the horizontal flux divergence approach by flying closed loops near Bakersfield, CA. By making concurrent measurements of the trace gases as well as the wind fields, we have reduced the uncertainty due to wind field in production rates.
Results: We find that the entire region is a source for both NO_2 and O_x'. NO_2 production

**Corresponding author: Email: rainer.volkamer@colorado.edu;*

is highest over the city (1.35 kg hr^{-1} km^{-2} NO_2), and about 30 times lower at background sites (0.04 kg hr^{-1} km^{-2} NO_2). NO_x emissions as represented in the CARB 2010 emission inventory agree well with our measurements over Bakersfield city (within 30%). However, emissions upwind of the city are significantly underestimated. The O_x' production is less variable, found ubiquitous, and accounts for 7.4 kg hr^{-1} km^{-2} O_x' at background sites. Interestingly, the maximum of 17.1 kg hr^{-1} km^{-2} O_x' production was observed upwind of the city. A plausible explanation for the efficient O_x' production upwind of Bakersfield, CA are favorable volatile organic compound (VOC) to NO_x ratios for O_x' production, that are affected by emissions from large oil and natural gas operations in that area.

Conclusion: The NO_2 and O_3 source fluxes vary significantly, and allow us to separate and map NO_x emissions and O_x production rates in the Central Valley. The data is probed over spatial scales that link closely with those predicted by atmospheric models, and provide innovative means to test and improve atmospheric models that are used to manage air resources. Emissions from oil and natural gas operations are a source for O_3 air pollution, and deserve further study to better characterize effects on public health.

Keywords: Active and passive remote sensing; LIDAR; AMAX-DOAS; fluxes, air pollution;

1. INTRODUCTION

Ozone (O_3) and nitrogen oxides (NO_x = NO + NO_2) are trace gases that are important components of air pollution. Health concerns of O_3 and NO_2 are related to respiratory illnesses such as chest pain, reduced lung function, asthma, emphysema whereas environmental concerns include reduced vegetation growth and acid rain. Due to these concerns both trace gases are recognized as air pollutants by air quality regulating agencies around the world, and are regulated by air quality standards and guidelines. The World Health Organization (WHO) air quality guideline recommends the standard to be set at 100 µg m^{-3} (~51 ppb) for O_3 (8 hour mean) and 40 µg m^{-3} (~21 ppb) for NO_2 (annual mean) [1]. The National Ambient Air Quality Standard (NAAQS) set by U.S. Environmental Protection Agency are 75 ppb for O_3 (8 hour maximum) and 53 ppb for NO_2 (annual mean) [2]. Similarly, the current air quality standard for the European Union are 120 µg m^{-3} (~61 ppb) for O_3 (8 hour maximum) and 40 µg m^{-3} (~21 ppb) for NO_2 (annual mean) [3]. Further, O_3 is a greenhouse gas that is relevant to climate discussions [4]. The lifecycles of O_3 and NO_x are intimately coupled, because NO_2 photolysis by sunlight drives photochemical O_3 production, while emissions of NO destroy O_3 to form NO_2. The sum of O_3 and NO_2 is called O_x, and is a conserved quantity as it implicitly accounts for the destruction of O_3 by NO (O_3 titration). Excess O_x is formed from the oxidation of volatile organic compounds (VOCs) in the presence of NO_x [5-7]. Fig. 1 shows a schematic diagram of photochemical O_3 production and evolution of NO, NO_2, O_3 and O_x concentrations upwind (I), within city limits (II) and downwind (III and IV) of an urban area. Different chemistry in these regions results in the characteristic spatial patterns in NO_x-O_3 distributions depicted in Fig. 1, which are: (1) Background O_3 present in the upwind region (I). (2) Emission of NO_x in the city limits (II), which leads to (3) O_3 removal via reaction with NO to produce NO_2 (titration reaction). (4) Photochemical production of O_3 from VOC/NO_x chemical cycles, which dominates downwind of the city center (III) and results in O_3 concentrations to accumulate. Further (5) the O_3 concentration does no longer accumulate in some distance downwind (IV), when NO_x has been oxidized to NO_y. NO_y is efficiently deposited or lost to aerosols resulting in insufficient NO_x to drive VOC-NO_x chemical cycles (NO_x limited region). Ultimately O_3 removal by photolysis and dry deposition leads to a slowly decreasing O_3 concentration here [6-8].

Due to their importance for air quality and human health, NO_2 and O_3 plumes from point sources and urban areas have been extensively studied. Previous studies have estimated NO_2 emission rates from point sources like power plants [9], urban areas [10-13], O_3 production rates in urban plumes [14,15], the amount of O_3 transported from urban areas and its impact on regional background O_3 [15], and the relationship between O_3, NO and NO_2 as function of NO_x in urban areas [16]. However, despite decades of research, models that predict O_3 formations have not been constrained by observations at the scale of cities and immediately downwind of cities. The comparison at the local scale is important, because of uncertain and changing emission of VOCs [17], NO_x [18], complicated transport [19-21] over cities and downwind of cities, and also uncertainties in non-linear chemistry that couples VOCs, NO_x and O_3. Such chemistry is heavily parameterized in current atmospheric models used to predict O_3. The net O_3 production by VOC oxidation is related to the conversion of NO to NO_2 by organic peroxy-and hydro peroxy radicals that are formed during the airborne oxidation of VOCs by atmospheric oxidants like OH, NO_3, O_3, and Cl radicals [22]. Under high NO_x conditions, the rate of O_3 production is limited by the availability of VOCs, while availability of NO_x controls the rate of O_3 production under low NO_x conditions [22-25]. For example, the testing of detailed chemical mechanisms of VOC oxidation using simulation chamber data [26,27], and field observations [28-31] often predict lower O_3 formation rates than that are actually being observed. The uncertainty in the chemistry of O_3 formation can be of similar relevance as uncertainties in emissions, and transport [30]. Further, transport of O_x across city, state and international borders causes possible non-attainment of O_3 levels at sites downwind [15,20,32] and the changing boundary conditions complicates enforcement of regulations.

Over the course of the last decade, emission control policies aimed at reducing ambient O_3 levels have resulted into NO_x reductions in North America and Europe [18,33-38]. NO_x sources in the troposphere are primarily related to anthropogenic emissions from on-road motor vehicles and power plants. With more than half of the world population now living in urban areas, cities have developed into hotspots for NO_x sources [18,33,34] and provide opportunities for NO_x reductions that are relevant on the global scale. This trend towards urbanization on global scales is unique in the history of mankind, and has the potential to change the planet. There is an increasing need for the development of analytical approaches that are effective at quantifying emissions of NO_x, provide experimental constraints to O_x production rates, and transport in order to refine atmospheric models that are used to manage air resources.

The primary objective of this study is to demonstrate the potential and feasibility of integrated use of passive and active remote sensing instruments and column observations to estimate the rate of NO_x emissions, and investigate the O_x production from an urban area. We use the mass conservation approach to estimate source strength for NO_2, and O_x from an urban area. Recently, ground based mobile differential optical absorption spectroscopy (DOAS) measurements have been used to estimate NO_x emissions from urban areas using this approach [10,11,13]. A similar approach has also been used to probe NO_x emission from megacities using satellites [12]. We have made simultaneous measurements of NO_2 vertical columns, O_3 and wind profiles for the first time from a research aircraft. The data set provides an opportunity to estimate production of individual species and investigate the conserved quantity, O_x, which could be significantly impacted by O_3 titration in NO_x source areas such as city centers. As a case study, data from a research flight on June 15, 2010 over Bakersfield, California is presented.

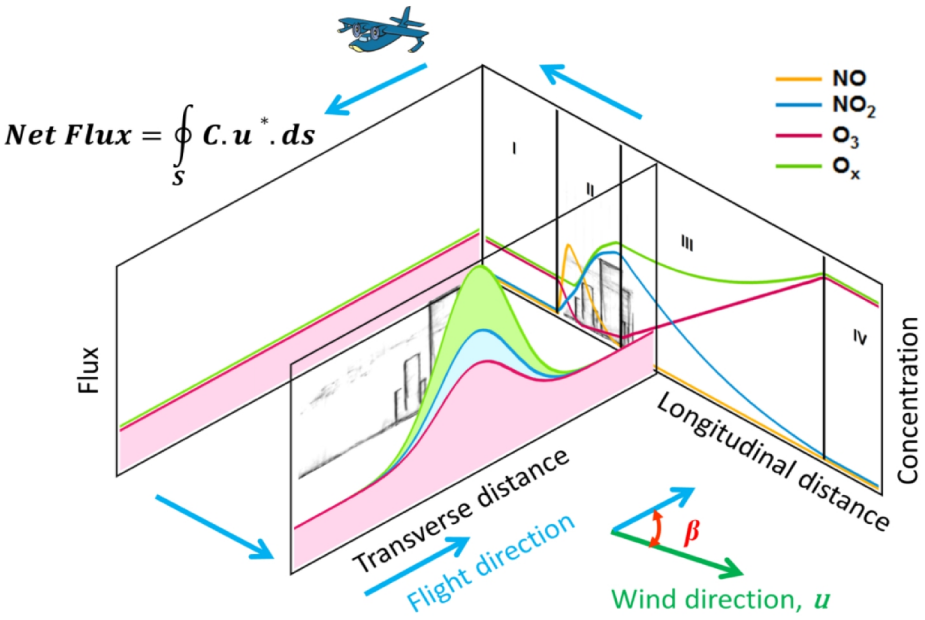

Fig. 1. Schematic diagram showing cross-section of ozone formation in an urban area under steady wind conditions and horizontal flux divergence measurements in a closed loop for source strength calculations. Evolution of NO (orange), NO_2 (blue), O_3 (maroon) and O_x (green) over different urban regions: (I) upwind, (II) urban center, (III) downwind and (IV) further downwind are also illustrated.

2. METHODOLOGY

We use a mass conservation approach to estimate the emission and production source strength of NO_2 and O_x. Neglecting the molecular diffusivity term in the mass conservation equation, the NO_2 and O_x source strengths within a given volume can be estimated from their time rate of change within the volume and the horizontal flux divergence across the boundaries enclosing the volume. We have conducted measurements of vertical columns of NO_2, O_3, and wind profiles aboard a research aircraft that flew box patterns over and near an urban area. Fig. 1 shows a conceptual schematic illustrating our approach for measuring NO_2 and O_x production rates.

Three remote sensing instruments namely (1) the University of Colorado Airborne Multi-Axis Differential Absorption Spectroscopy instrument (CU AMAX-DOAS), (2) the National Oceanic and Atmospheric Administration (NOAA) Tunable Optical Profiler for Aerosol and Ozone (TOPAZ) lidar and (3) the National Center for Atmospheric Science (NCAS) Doppler lidar were deployed aboard the NOAA Twin Otter research aircraft. The configuration of the three instruments aboard the Twin Otter is shown in Fig. 2. A total of 52 research flights were conducted over the course of two months (May 19-July 19, 2010) as part of the California Research at the Nexus of Air Quality and Climate Change (CalNex) [39] and the Carbonaceous Aerosol and Radiative Effects Study (CARES) [40] field campaigns in California during summer 2010. Most of the flights were focused on the Los Angeles basin

and Greater Sacramento area. More details on the individual Twin Otter research flights can be found in Ryerson et al. [39]. One of the foci of this deployment was to constrain the emission and production of NO_2 and O_3 upwind, within and downwind of urban areas.

2.1 AMAX-DOAS

The CU AMAX-DOAS instrument [41,42] uses scattered sunlight as the light source (passive remote sensing). The scattered sunlight spectra are analyzed for the presence of absorbers like NO_2, glyoxal (CHOCHO), formaldehyde (HCHO) and oxygen dimer (O_4) among others using the DOAS method [43]. The instrument and its performance during CalNex and CARES field campaigns are described in detail in Baidar et al. [42]. Briefly, a telescope pylon is mounted on the outside of the window plate of the aircraft and includes a rotatable prism to collect scattered photons from different elevation angle (EA) i.e. angle relative to the horizon. Spectra collected from different EA contain information from different layers in the atmosphere and hence can be used to obtain information about vertical distribution of trace gases. The collected photons are transferred to a spectrometer / charge coupled device (CCD) detector system via optical glass fiber bundle. Here we will only present data from nadir viewing geometry from the flight over Bakersfield.

The measured spectra were analyzed, for NO_2 in a wavelength range from 433 to 460 nm, against a fixed zenith reference spectrum recorded during the same flight in a clean environment and flying at relatively high altitudes (3 – 5 km; 3.5 km for this flight). Zenith spectra were recorded frequently, and are used to correct for stratospheric NO_2 contributions and NO_2 above the aircraft. The nadir NO_2 differential slant column densities (dSCDs) are observed below the plane and correspond to the average integrated difference in concentration of the absorber along the light path with respect to the reference. Since most of the NO_2 sources in an urban environment are located close to the surface, the retrieved nadir dSCD was considered to be the boundary layer slant column ($dSCD_{bl}$). NO_2 nadir measurements were performed every 20-25 s and hence NO_2 data points are available every ~1.5 km horizontally. For the conversion of nadir NO_2 $dSCD_{bl}$ into boundary layer vertical column densities, VCD_{bl}, the geometric Air Mass Factor (AMF_{geo}) approximation was applied.

$$\mathrm{AMF_{geo}} = \frac{1}{1+\frac{1}{\cos(\mathrm{SZA})}} = \frac{\mathrm{SCD_{bl}}}{\mathrm{VCD_{bl}}} \qquad (1)$$

Here, SZA refers to solar zenith angle at the time of the measurement. This approach is in good agreement with explicit radiative transfer calculations for California while flying between 2 and 4 km. Radiative transfer calculations for the conditions of the Bakersfield case study (flight altitude: 2 km, SZA: <25º), and comparisons with ground based vertical columns consistently reveal the uncertainty in AMF_{geo} to be less than 7% [42]. The overall uncertainty in NO_2 VCD for the Bakersfield case study is estimated to be around 9% (AMF_{geo} : <7%, NO_2 cross-section: ~5%, DOAS fit: ~3%) [42,44].

2.2 TOPAZ

NOAA's nadir-looking TOPAZ differential absorption lidar is a compact, solid-state-laser-based O_3 lidar that emits pulsed laser beams at three tunable wavelengths in the UV spectral region between about 285 and 300 nm [45]. The differential attenuation of the three wavelengths due to O_3 permits the retrieval of O_3 concentration profiles along the laser beam path [46]. TOPAZ O_3 profiles were computed every 10 s (or about 600 m horizontally) with a

vertical resolution of 90 m. The ozone profiles extend from about 400 m beneath the plane to near the ground. O_3 values in the lowest two measurement bins (lowest 180m) above ground level (AGL) are typically not used because of poor signal to noise ratio.

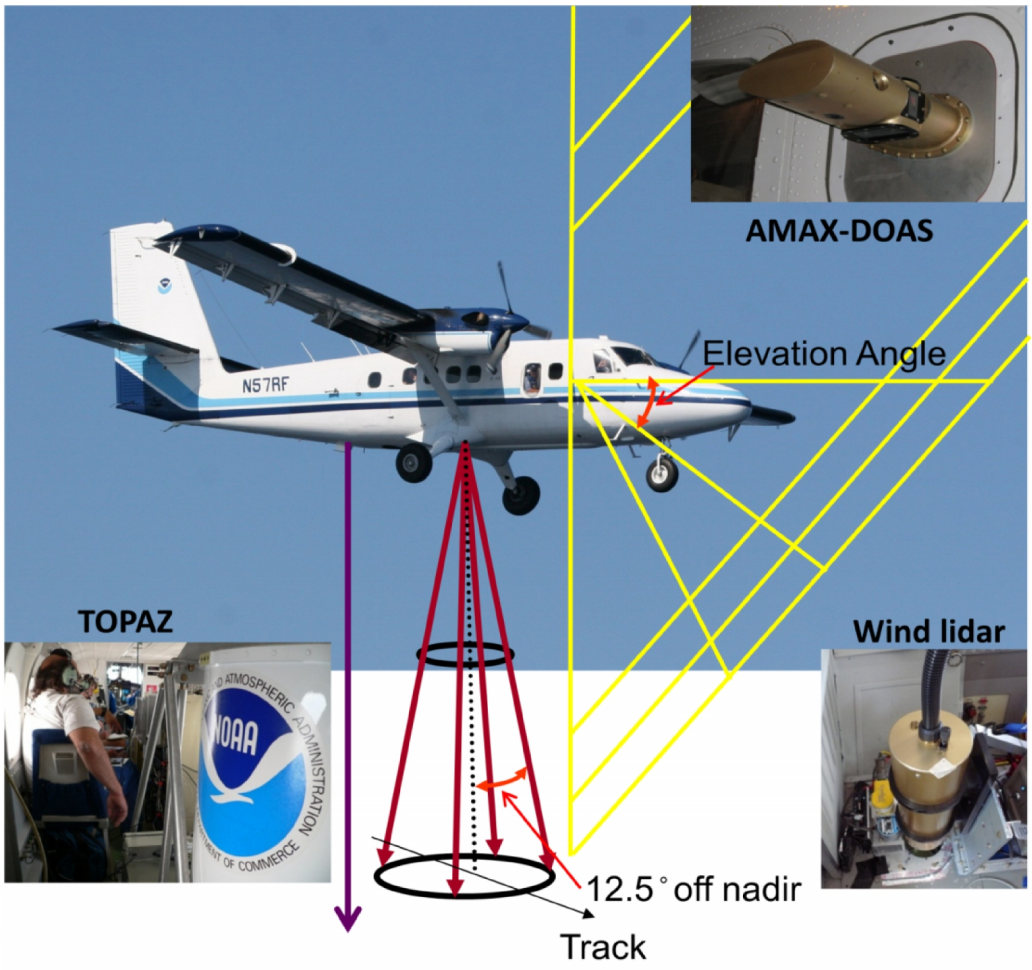

Fig. 2. Instrumental setup of CU AMAX-DOAS, NOAA TOPAZ lidar and NCAS Doppler wind lidar aboard the NOAA Twin Otter research aircraft during CalNex and CARES field campaigns. The yellow, purple and maroon lines represent viewing geometry of CU AMAX-DOAS, NOAA TOPAZ lidar and NCAS Doppler wind lidar respectively. The three instruments are also shown in the insets.

The TOPAZ lidar also provided aerosol backscatter profiles for the longest (and least absorbed by O_3) of the three emitted wavelengths near 300 nm. The time resolution of the aerosol backscatter profile measurements is the same as for O_3, but the vertical resolution is much finer at 6 m. We used these highly resolved lidar backscatter profile data to retrieve boundary layer height (BLH) by employing a Haar wavelet technique [47]. This approach is based on the (often valid) assumption that the aerosol concentration is higher in the boundary layer (BL) than in the lower free troposphere (FT). The altitude at which the strongest aerosol gradient is found by the wavelet technique is used as an estimate of the

BLH. At times, the contrast in aerosol backscatter between the BL and the overlying FT is not sufficient to yield reliable results, and the BLH is not reported for such scenarios.

We used the BLH estimates and O_3 profiles measured with the TOPAZ lidar to compute O_3 column data integrated over the depth of the BL. To fill in data gaps in the O_3 profiles close to the ground, we averaged the ozone measurements in the lowest two gates with usable data (typically 200 - 300 m AGL) and extrapolated this value to the ground. We then integrated these extrapolated ozone profiles from the surface to the top of the BL to yield BL O_3 column density along the flight track at 10-s resolution. When BLH estimates were not available from the backscatter profile for a given O_3 profile, BLH was interpolated from adjacent measurements to compute O_3 vertical column over the BLH. TOPAZ O_3 measurements have been extensively compared to and agree well (±2-9%) with in situ airborne O_3 observations [48].

2.3 Doppler Wind Lidar

Information on the wind structure below the aircraft was provided by the NCAS Doppler lidar [49] mounted in the Twin Otter cabin. The lidar measures the Doppler shift of radiation scattered from atmospheric aerosol particles to estimate the component of wind along the lidar line of sight. Typical precision of the lidar radial wind measurements under acceptable aerosol loading is better than a few tens of cm s^{-1}. The lidar was mounted in the cabin with the beam transmitted vertically through a small camera port located on the underside of the aircraft (Fig. 2). In order to measure the horizontal component of the winds a rotatable refractive wedge mounted in the port directed the beam to 12.5º off nadir. The original scanner design included two wedges, which provides greater beam deflection and enables vertical pointing; however poor optical quality of the wedges forced us to eliminate the second wedge to reduce total attenuation through the scanner.

During flight operations the wedge was rotated to four different azimuth angles (45, 135, 225, 315º) relative to the flight track. Dwell time at each azimuth angle was 1 s for most of the Doppler measurements during CalNex. A complete rotation among the four azimuths required 8 s, including the time required to rotate the wedge to a new position. At the nominal Twin Otter speed of 60 m s^{-1} a complete 4-beam scan was completed about every 500 m. Vertical resolution of the lidar wind measurements was roughly 50 m.

Information on aircraft speed and orientation was obtained from the CU AMAX-DOAS motion compensation system [42]. Additionally, we used the surface return at the four look angles, for which the only Doppler shift results from motion of the aircraft, to provide additional information on aircraft orientation and velocity. For the case described here, a 19-beam running average of the radial wind estimates at each of the four azimuth angles was computed to improve precision of measurements. After removal of the Doppler shift induced by aircraft motion, the velocities from the four azimuth angles were combined in a least-squares type algorithm to estimate the mean wind speed and direction in each of the 50 m range gates where backscatter was high enough to provide a strong signal. The wind speed and direction were averaged up to the BLH before further calculations of horizontal flux. The uncertainty in the wind measurement is estimated to be around 6% based on the difference between wind retrievals from a longer (19-beam) and a shorter (3-beam) running average wind fits.

2.4 Bakersfield Case Study

Bakersfield is a city located in the southern part of the Central Valley, CA, surrounded mostly by agricultural area and oil and natural gas operations. In the summer months, wind blows predominantly from the northwest down the valley providing steady wind conditions necessary for the method presented here. The Bakersfield area also makes for an interesting case study to probe NO_2 and O_x production from a large city influenced by intense agriculture and petrochemical production. In particular, we have probed (i) background air unaffected by urban anthropogenic emissions, (ii) air upwind, influenced by agricultural and petrochemical production, (iii) urban emissions from the city, and, (iv) the chemical evolution downwind, after it is perturbed by urban emission inputs.

The flight plan of the Twin Otter on June 15, 2010 (see Fig. 3) was designed to interrogate NO_x emissions and constrain the O_3 production from different source regions enclosed by "boxes" by applying the horizontal flux divergence approach. The flight plan included an enclosed box, over areas with no major emission sources, in the northwest of Bakersfield to characterize the background conditions (Box A; see Fig. 4). Two boxes (Box C and D; D is twice the size of C) were flown over the city of Bakersfield to constrain emissions/productions from the city. In order to contrast NO_2 and O_3 production upwind and downwind of Bakersfield, two additional boxes (Box B and E) were created by interpolating the measured NO_2, O_3 and wind data for the western legs (shown as diamonds in Fig. 4). A larger trapezoid (Box F) was flown, connecting the three boxes, and enclosing the entire greater Bakersfield region. It took approximately 15, 13 and 18 minutes to complete boxes A, C and D respectively while the larger Box F took ~75 minutes. The entire box patterns were flown at a constant altitude (~2000 m above sea level), well above the BL. Details related to the times and meteorological conditions encountered for each boxes are summarized in Table 1.

Table 1. Meteorological conditions on June 15, 2010 for the closed boxes flown near Bakersfield, CA

Box	Area (km x km)	Time (UTC)	Wind speed (m/s)	Wind direction (º)	Boundary layer height (m, AGL)	
			mean ± sdev	mean ± sdev	min	max
A	20 x 14	20:24-20:38	5.6 ± 1.7	283 ± 44	1005	1548
B	20 x 19		4.3 ± 1.6	314 ± 41	760	1425
C	20 x 9	19:41-19:54	4.1 ± 1.5	317 ± 49	936	1425
D	20 x 18	21:07-21:25	4.7 ± 0.9	317 ± 26	1049	1481
E	20 x 18		3.0 ± 0.8	328 ± 27	1066	1450
F	67 x 56	19:54-21:11	3.3 ± 1.8	313 ± 41	760	1524

2.5 Horizontal Flux and Source Strength

For each transect, the gas flux at a point, *x* along the flight path is obtained by multiplying the column measurement at that location, *column(x)* by the corresponding wind speed averaged over the BLH, $u^*_{avg}(x)$ [10,11]. The flux calculation through a surface area, *A* is shown in equation 2:

$$\int \vec{f}.d\vec{A}_{area} = \int_{x1}^{x2}\int_{0}^{BLH} conc(z).u^*(z).dzdx = \int_{x1}^{x2} u^*_{avg}(x).column(x)dx \quad (2)$$

Where *J* corresponds to flux at any location, *x* to the flight direction, *z* to the altitude, *u** to the wind speed orthogonal to the flight direction *(x)* and is assumed to be constant over the BLH, u^*_{avg} to wind speed averaged up to the BLH, and

$$column = \int_0^{BLH} conc(z).dz \quad (3)$$

$$u^* = u.\sin(\beta) \quad (4)$$

Here *u* is wind speed and *β* is angle between wind direction and flight heading.

Flux measurement in a closed loop can be used to estimate source strength within the enclosed volume [10,11]. The general continuity equation in the integral form is given in equation (5) and is the basis for the source strength calculation. It involves three terms: source, flux divergence and rate of change of concentration.

$$Q_{net} = \oint_S \vec{J}.d\vec{A}_{area} + \int_{Vol} \frac{\partial conc}{\partial t} dV_{vol} \quad (5)$$

i.e. the net source strength of an enclosed volume, Q_{net} is the sum of fluxes through all areas along the closed loop (incoming and outgoing) and change in concentration inside the volume.

We assumed that the time dependence of concentration in the enclosed volume is zero over the time scale of our measurement. Our measurements were performed during the midday when rate of change of NO_2 and O_3 concentration in the Bakersfield area is very small (see Fig. 5). Hence, we neglected the second term on the right hand side in equation (5). We also assumed that the net vertical exchange and deposition are negligible over the timescale of our measurement. Hence, the net flux i.e. the difference in fluxes entering and leaving the enclosed volume through the walls gives the source strength for the species of the particular enclosed area at the time of the measurement.

2.6 Daily NO_x Emission

Daily NO_x emission was estimated based on the computed NO_2 source strength, diurnal profile of NO_2 and the NO_x to NO_2 ratio measured at the California Air Resource Board (CARB) monitoring station at Bakersfield. It is computed as:

$$NO_x\ emssion\ = \sum_{t=10}^{20} E.\frac{[NO_2(t)]}{[NO_2(t_0)]}.\frac{[NO_x(t)]}{[NO_2(t)]} \quad (6)$$

Where *E* is the computed NO_2 production rate from (5), *t* is hour of the day, t_0 is the hour of our measurement. Therefore, the daily NO_x emission is the sum of product of measured NO_2 emission rate at time t_0, ratio of NO_2 at time *t* and t_0 and ratio of NO_x to NO_2 at time *t* over the course of the day. In order to minimize potential bias created due NO_x accumulation overnight, we only calculated daily NO_x emission for the period when NO_2 and NO_x measurements at the CARB station were stable (10:00-20:59 PST). Fig. 5 shows NO_2, NO_x and O_3 mixing ratios measured hourly at the Bakersfield CARB monitoring station on that day. The time period of our measurement and time frame for the daily NO_x emission calculation are also shown in Fig. 5.

3. RESULTS AND DISCUSSION

The measurement on June 15, 2010 over Bakersfield, CA was performed at mid-day when the change in NO_2 and O_3 concentration is very small, providing chemically stable conditions most suitable for source strength calculations. This is supported by NO_2 and O_3 measurements at the CARB monitoring station at Bakersfield (see Fig. 5). Column O_3, BLH from the NOAA TOPAZ lidar, column NO_2 from the CU AMAX-DOAS, and wind speed and direction from NCAS Doppler lidar are shown in Fig. 3. Fig. 3a shows the BLH at the time of the measurement retrieved from TOPAZ backscatter profiles. In general, the highest O_3 and NO_2 VCDs were measured in the southeastern corners of the boxes especially for boxes with significant emission sources (Fig. 3b and 3c), consistent with the prevailing wind conditions. We calculated NO_2 and O_x production rates for the six boxes.

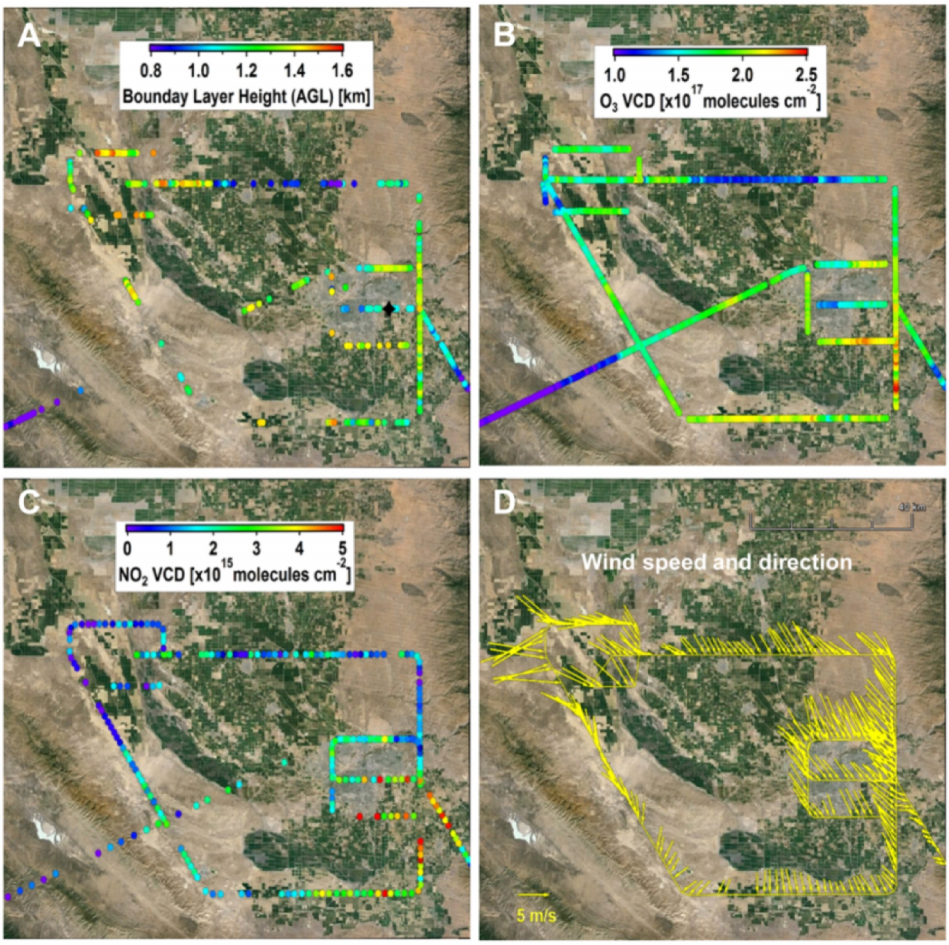

Fig. 3. Maps of (A) Boundary layer height (BLH) above ground level, (B) O_3 vertical columns up to the BLH, (C) NO_2 vertical columns and (D) wind speed and direction from the flight over Bakersfield, CA on June 15, 2010. BLH and O_3 columns were measured by NOAA TOPAZ lidar, NO_2 vertical columns by CU AMAX-DOAS and wind speed and direction by NCAS Doppler wind lidar. Black diamond on A shows the location of CalNex Bakersfield supersite.

The wind speed and direction and BLH during the time of measurements for different boxes are given in Table 1. The wind was blowing predominantly from the northwest and provided ideal conditions as horizontal flux divergence measurements require steady wind fields (also see Fig. 3d). The variability in wind speed and direction was larger for upwind boxes (A and B) compared to downwind boxes (D and E). The BLH range for boxes D and E were also smaller compared to other boxes. The observed BLH variability is most likely a combination of land use changes (irrigated fields vs. dry land vs. urban heat island) and the fact that upslope flow over the foothills east of Bakersfield favor BLH growth, while strong subsidence over the middle of the valley acts to suppress BL growth. We use the BLH variability to estimate the amount of BL air column susceptible to exchange with the FT (see Section 3.1.). Since all the parameters needed to quantify flux are constrained by measurements here, the horizontal variability in BLH does not pose a limitation to our approach. Notably, the variability of BLH remains difficult to predict by atmospheric models, and warrants further investigation.

Background corrected O_x (O_x' from here on) column up to the BLH, computed as the sum of NO_2 and background corrected O_3 columns, is shown in Fig. 4. Background correction for O_3 is needed as we are interested in the source strength of the area at the time of measurement i.e. the amount that is being produced locally. The background correction also minimizes any potential biases due to BL-FT exchange in case of strongly varying BLH. If BLH is constant over a box, then background correction is not necessary, because incoming and outgoing background fluxes are the same and cancel each other. Note that we measure column amount of O_3 and NO_2. Background O_3 levels were calculated based on the mean O_3 concentration over the BLH in the northwestern corner of the Box A (see Fig. 4). We note that 'background' air in the Central Valley is affected by transport of pollution emitted upwind; indeed we find significant production of O_x' in Box A. However, low and similar amounts of NO_2 are transported into and out of Box A, and net production of measured species is the lowest observed anywhere. We find no evidence for major emission sources within Box A. The mean and the standard deviation of the background O_3 concentration was $1.20 \pm 0.03 \times 10^{12}$ molecules cm^{-3} (48.8 ± 1.2 ppbv, 1ppbv = 2.46×10^{10} molecules cm^{-3}). It was assumed that this background O_3 concentration is representative of the entire area. A background O_3 column was calculated for each measurement point along the flight track by multiplying this O_3 concentration with BLH at that location. This background column was then subtracted from the measured O_3 column to determine O_3', which corresponds to the excess O_3 column at each point along the flight track. NO_2 VCDs were used without further corrections as they were below the detection level over that area (4.2×10^{14} molecules cm^{-2}, ~130 pptv). The average column NO_2 to O_x' partition ratio increased from 2% over the background site to 7% over the city of Bakersfield. Thus, NO_2 gas forms a significant portion of O_x' over the urban area and would result in a bias if O_3 production rates were calculated instead of O_x. By investigating O_x' we eliminate the uncertainty due to titration of O_3 by NO to form NO_2 in the NO_x source regions.

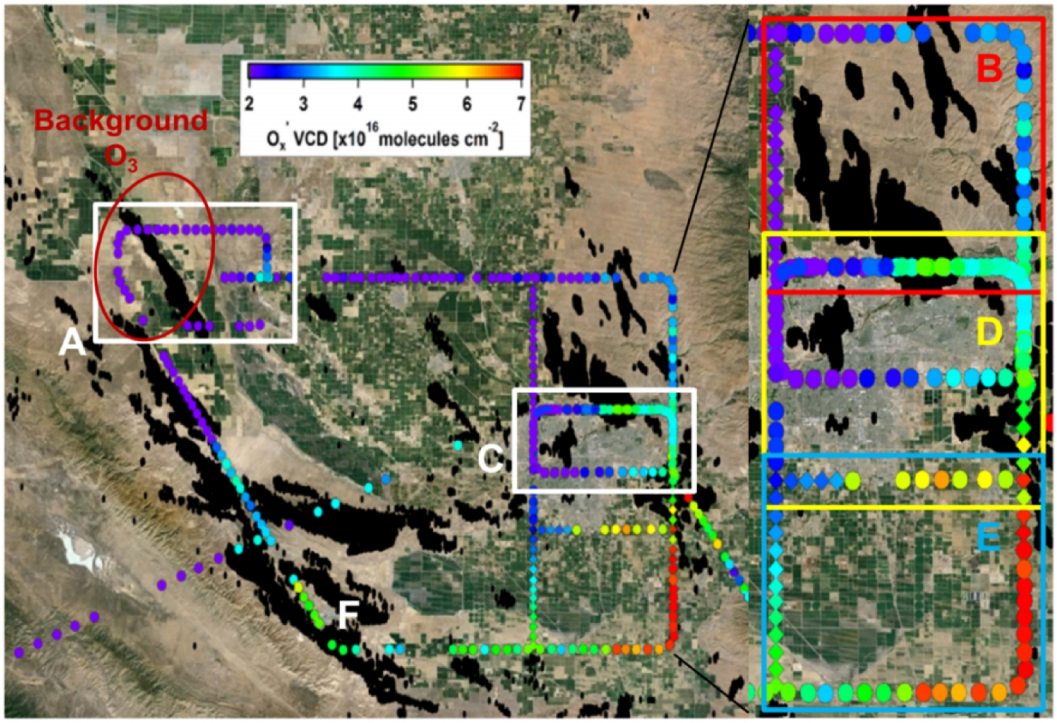

Fig. 4. Map of O_x' vertical columns up to the BLH. Rectangles represent different boxes flown over Bakersfield: (A) upwind background area, (C) over the city, and (F) over the entire area. Colored rectangles in the inset highlight three boxes: (B) upwind, (D) over the city, and (E) downwind. Box B and E were created for comparison purposes by interpolating the western legs. Interpolated data are shown as diamonds. Black areas in the map show active oil and gas wells in the region.

The minimum, maximum and mean mixing ratios of NO_2 and O_3 for each box are also given in Table 2. The average NO_2 and O_3 concentrations were lowest for the background box. The NO_2 concentrations show higher variation within a box as well as between the boxes, indicating highly local NO_2 sources in the area. The mean O_3 does not vary much between the boxes (see Table 2). Notably, the maximum O_3 concentrations were observed to be generally related to the O_x' production rates in the box upwind of a given box, which is expected. Both O_3 and NO_2 showed the highest average concentration over the downwind box (E). Considering that the production rates are lower compared to the boxes upwind (B and D), there could be some accumulation of NO_2 and O_3 taking place in this box.

The enclosed areas are sources for both NO_2 and O_x' for all the boxes investigated. The NO_2 and O_x' production rates calculated for different boxes are given in Table 2. The production rates were calculated using equation (5) and have been normalized for the area of the boxes so that they can be directly compared to each other. As expected, the background, Box A, has the lowest production rate for both NO_2 and O_x'. The NO_2 production rate in the background box was 0.04 kg hr^{-1} km^{-2}. The NO_2 production rate was highest for Box D and amounts to 1.35 kg hr^{-1} km^{-2} above Bakersfield. This is consistent with the present knowledge that urban city limits are the dominant source for NO_x emissions in California [18].

Boxes C and E, located in the northern half of Box D, and immediately downwind of Box D respectively, show about 13 times lower NO_2 production rate, indicating that the NO_2 sources from the urban area are highly localized. Interestingly, the site upwind of Bakersfield (Box B) was also found to be a significant source for NO_2 compared to the downwind site (Box E).

Table 2. NO_2 and O_3 mixing ratios and NO_2 and O_x' production rates normalized by area of the boxes for each box near Bakersfield, CA on June 15, 2010

Box	Mixing ratio[1]		Production rates[4]	
	NO_2 (pptv)	O_3 (ppbv)	NO_2[2]	O_x'[3]
	min / max / mean	min / max / mean	($x10^{-2}$ kg hr^{-1} km^{-2})	(kg hr^{-1} km^{-2})
A	22 / 864 / 298	45 / 59 / 51	4 ± 8	7.4 ± 0.6
B	38 / 951 / 497	47 / 62 / 58	60 ± 6	17.1 ± 0.8
C	145 / 2425 / 852	47 / 67 / 58	11 ± 15	11 ± 2
D	149 / 1554 / 694	52 / 68 / 60	135 ± 12	13 ± 1
E	563 / 1948 / 1183	56 / 76 / 66	12 ± 10	11 ± 1
F	22 / 1948 / 582	45 / 76 / 59	39 ± 1	9.4 ± 0.1

[1]Mixing ratio is calculated assuming that the NO_2 and O_3 are uniformly distributed over the boundary layer. Conversion: 1 pptv = 2.46 x 10^7 molecules cm^{-3} and 1 ppbv = 2.46 x 10^{10} molecules cm^{-3}.
[2]Molecular weight of NO_2 (MW_{NO2}) =46 g/mole
[3]Molecular weight of O_x ($MW_{Ox'}$) = 48 g/mole
[4]Error in the production rates represents total propagated measurement uncertainty. Details are provided in Section 3.1.

The O_x' production rate for the background box was 7.4 kg hr^{-1} km^{-2}, the lowest of all boxes. Box A likely represents the O_x' production rates for regions in the Bakersfield area that are not affected directly by the urban emissions. Notably, the NO_2 production from within box A was the lowest we have observed in this case study. However, our approach does not attempt to make a correction for NO_2 losses due to photochemistry and deposition, and as such the reported NO_2 production has to be considered a lower limit. While the measured NO_2 flux was essentially zero within error of the measurements, this indicates that comparable amounts of NO_2 enter and exit the box, and that enough NO_x was present to produce O_3. This was confirmed by our observations of elevated O_x production in box A. Interestingly, the O_x' production rates over the Bakersfield city limit (Box C and D) and downwind site (Box E) only showed small enhancement (< factor of 1.75) over the background O_x' production rate. This indicates that even though the NO_2 levels in the wider area surrounding Bakersfield are relatively small (~330 pptv), there is enough NO_x to sustain photochemical O_x' production in the entire region. Surprisingly, the upwind box (Box B) was found to have the largest O_x' production rate (17.1 kg hr^{-1} km^{-2}, 2.3 times that of Box A). The O_x' production rate in Box B was 133% that of urban Box D while the NO_2 production was only about 40% of the urban box. A plausible explanation for our observation of efficient and high O_x' production from Box B could be from enhanced VOC levels due to large oil and natural gas operations in the area, creating favorable conditions for enhanced O_3 production (high VOC/NO_x ratio). Oil and natural gas production is a source for atmospheric methane, a greenhouse gas, and other more reactive hydrocarbons as well as NO_x. The observed elevated emissions of NO_x in box B indicate emissions are active in this area. While higher NO_2 is likely to contribute to the higher O_3 production rate, additional VOC emissions are needed to explain such a high increase in the O_3 production rate. We are unable to conclude about additional VOC sources from our data at this point, but note that some emissions of reactive hydrocarbons are expected from the oil and natural gas production in the area that

could help accelerate O_3 formation. Notably, the O_3 produced within Box B was only partially transported into the downwind boxes, where lower O_3 production rates were observed. This decrease in O_3 production rates downwind of Box B are probably related to higher NO_2 concentrations, and a different VOC/NO_x ratio as air mixes with urban sources. The net effect of the added emissions from urban sources was a lowering of the O_3 production rates. The black areas in Fig. 4 represent active oil and gas wells in the region [50].

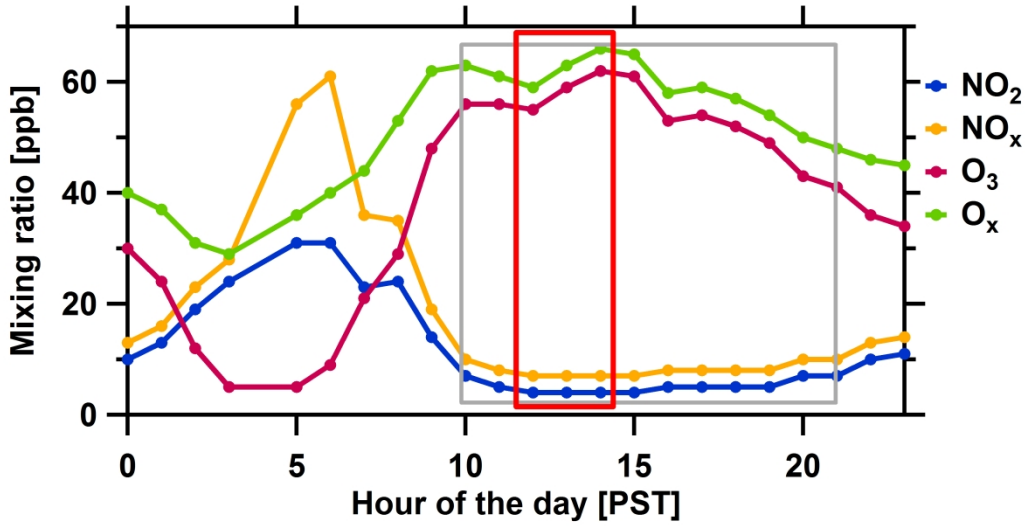

Fig. 5. Diurnal variation of NO_2, NO_x, O_3, and O_x measured at the Bakersfield CARB monitoring station on June 15, 2010. The red and grey rectangles represent the timeframe of our measurement and time period used for daily NO_x emission calculation respectively.

The measured NO_2 production rates were used along with the diurnal profile of NO_2 and NO_x measured at the CARB monitoring network station of Bakersfield (see Fig. 5) to provide an estimate of daily NO_x emissions in Table 3. We only considered the daylight hours (10:00-20:59 PST) when the measured NO_2 and NO_x at the CARB station were stable in order to minimize potential bias due to NO_x accumulation overnight. The uncertainty in Table 3 only considers error in measured production rates and does not include spatial and temporal variability in NO_x and NO_2 across the region. The daily NO_x emission from Bakersfield was estimated to be around 10.7 metric tons for June 15, 2010 from 10:00-20:59 PST, compared with 13.5 tons NO_x for the same time frame in CARB 2010 emission inventory (CalNex-2010 modeling inventory) [51]. There is a mismatch in the location of NO_x emissions within Bakersfield. Our measurements suggest that the large portion of the emission occurs in the southern half of Box D. Note that NO_x emissions of Box C were also part of Box D (i.e., form the northern half of Box D). Emissions in Box C were comparatively very small. In contrast, emissions from Box C form a significant portion of overall emission of Box D in the CARB 2010 emission inventory. The NO_x emissions for the entire study area (Box F: 32.1 tons) were comparable to those in the CARB 2010 emission inventory in the same area (29.2 tons). However, there are differences in the locations of the NO_x emissions here as well. The background NO_x emissions are higher in the emission inventory whereas emissions over the oil and natural gas operations are significantly underestimated. Table 3 also compares hourly emission rates for the hour of our measurement. The measured emissions were lower

for all the boxes except for the upwind box, B. Considering that the daily emission estimates are in better agreement compared to the hour of measurement, there is a discrepancy in the timing of NO_x emission in the emission inventory. The diurnal profile of NO_2 and the NO_x to NO_2 ratio varies between days as well as seasons and hence we do not attempt to scale up to the yearly NO_x emission. However with regular flights over different times of the day and course of different seasons, the combination of active and passive remote sensing has the potential to constrain and improve NO_x emissions in emission inventories.

Table 3. Daily and hourly NO_x emissions calculated for June 15, 2010 from (i) using derived NO_2 production rate and NO_x and NO_2 diurnal profiles measured at CARB monitoring station at Bakersfield, CA and (ii) NO_X emissions from CARB 2010 emission inventory for that day. Errors represent error due to uncertainty in NO_2 production rates

Box	NO_x Emissions[1] (metric tons)			
	This work		CARB 2010 emission inventory	
	Daily[2]	Hourly[3]	Daily[2]	Hourly[3]
A	0.2 ± 0.5	0.02 ± 0.04	1.1	0.11
B	5.1 ± 0.5	0.40 ± 0.04	1.1	0.11
C	0.4 ± 0.6	0.03 ± 0.05	10.6	1.05
D	10.7 ± 0.9	0.85 ± 0.07	13.5	1.33
E	0.9 ± 0.8	0.07 ± 0.06	2.2	0.22
F	32.1 ± 0.9	2.56 ± 0.07	29.2	2.91

[1]Molecular weight of NO_x (MW_{NOx}) = 46 g/mole.
[2]Daily = 10:00-20:59 PST.
[3]Hourly = hour of our measurement

3.1 Error Estimates

Error in calculated fluxes and source strengths are a function of uncertainties in the measurements of individual species, winds, uncertainties about sinks (dry deposition and oxidation), and the variability of atmospheric state. Previous source strength calculations have found the uncertainty in the wind to be the largest source of error as it was not measured concurrently [10,11]. The uncertainty in the wind measurements is estimated to be around 6%. Thus, the uncertainty in the wind measurement itself has a relatively small effect on the production rates in our study. This uncertainty is very likely not representative of wind variability within the boxes but the variability in wind are captured as part of individual wind measurements.

The overall uncertainty in NO_2 VCD is ~9%. The contributions of different error sources in NO_2 VCD uncertainty is given in Section 2.1. It is assumed that all of NO_2 were located inside the BL. Based on the amount of NO_2 above the BL in the vertical profile through the city center (see Fig. 6) we estimate this leads to a systematic error of around a few percent. The lidar O_3 profile measurements at 90 m vertical resolution have an error of typically 6-10% and can be improved by integration and averaging [45,48]. O_3 data were integrated vertically (~10 points) and horizontally (2-3 points) for flux calculations at each location. As a result, the statistical uncertainties in the integrated O_3 are reduced to ~2%. O_3 data to the ground were extrapolated from measurement at lowest two gates assuming a well-mixed BL (see section 2.3). Based on the difference between measurement at the CARB stations and extrapolated values, we estimate this systematic error to be around 5%. The uncertainty in BLH retrieval for TOPAZ backscatter profile is ~7%. Considering the standard deviation of

background O_3 concentration (~4%), BLH uncertainty, O_3 column uncertainty and NO_2 column uncertainty, the overall error in the O_x' column is ~8%. Thus the total measurement uncertainty in the individual flux measurement is ~10-11%. The error for production rates of NO_2 and O_x' tabulated in Table 2 represents the overall uncertainty due to propagated error in individual column of the species and wind speed and direction for each box.

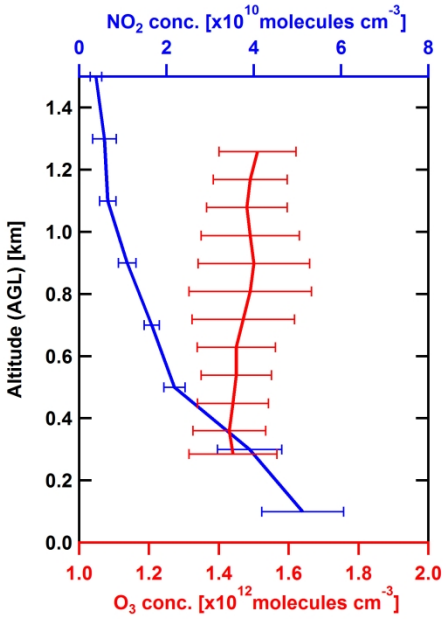

Fig. 6. Mean O_3 profile measured by NOAA TOPAZ lidar for Box D and NO_2 profile measured by CU AMAX-DOAS from a low approach at Bakersfield airport. Error bars for O_3 profile is the standard deviation of the mean and NO_2 shows measurement uncertainty.

Vertical transport, atmospheric sinks and chemical transformations over the transport time between source and sampling regions are other potential sources of errors in the measured production rates for NO_2 and O_x'. Our approach assumes that all transport through the enclosed box occurs horizontally. Entrainment flux is a product of entrainment velocity (w_e) and the difference in trace gas concentrations between the FT and the BL (ΔC) ($E_{flux} = w_e \times \Delta C$). To constrain the magnitude of potential vertical flux, we have used the rate of BLH growth as the entrainment velocity. This neglects the potential contribution of large-scale, mean vertical velocity and BLH advection. The northern legs for Box C and D overlap in location, but were flown ~90 minutes apart and provide an opportunity to calculate the BLH growth rate. It was estimated to be 1.2 cm s^{-1}. NO_2 and O_3 concentrations were determined from the vertical profiles obtained from the low approach over the Bakersfield airport (see Fig. 6). We estimate the vertical flux to be 2.30 x 10^{-3} kg km^{-2} hr^{-1} for NO_2 and 0.21 kg km^{-2} hr^{-1} for O_x' for Box D. Hence, the potential error due to vertical transport is likely to be smaller than 2%.

Typical dry deposition velocities, w_d, for O_3 and NO_2 in the continental environment are 0.4 and 0.1 cm s^{-1} respectively [6,7,52]. We calculated the depositional flux as $D_{flux} = w_d \times C$, where C is the trace gas concentrations at the lowest layer. This could result in error of ~

10% in the O_x' and ~1% in the NO_2 production rates. For an air mass transport time of 1 hour (between production and measurement), Ibrahim et al. [10] estimated the error in the production rate due to chemical transformation of NO_x, based on average atmospheric NO_x lifetime, to be around 10%. Considering that the transport time for our conditions is around 0.5 hour, we estimate the error due to chemical transformation of NO_2 to be less than 5%. The atmospheric lifetime of O_3 is more than 3 times that of NO_x. Hence, we estimate the error in O_x' production rate due to chemical transformation to be smaller than 2%. Thus, the potential error due to entrainment, dry deposition and chemical transformation is in the same order as the total measurement uncertainty in the production rates.

We observed very high local variation in BLH and this could also potentially result in error in the calculated production rates. The BLH variability makes the air column susceptible to exchange with the FT via horizontal transport. We have tried to bind the magnitude of this exchange in two ways: Method A calculates it as a product of the relative amount of air column (with respect to the average) susceptible to this exchange based on the difference in the average BLH measured for the upwind and downwind legs and our measured production rates; Method B calculates the same number based on the maximum and minimum BLH, assuming they occur equally frequent within each box. This is likely an upper limit estimate of such transport, since BLH is something in between most of the time. Note that we only know the BLH along the edge of the boxes and not within the boxes. We find that the uncertainty due to this potential FT exchange accounts for 1-8% (method A) of the overall horizontal flux. Method B yields 15-30% as an upper limit for FT exchange. To our knowledge the horizontally variable BLH as a mechanism for BL-FT exchange has not previously been studied, and deserves further investigation. We consider the error in horizontal fluxes from method A to be most likely representative of uncertainty in the production rates listed in Table 2 due to such an exchange.

4. CONCLUSION AND OUTLOOK

We demonstrated the feasibility of co-deployed active and passive remote sensing instruments aboard a research aircraft to study NO_x emissions and O_x production rates out of an urban area. NO_2 vertical column, O_3 vertical profile and wind profile measurements aboard the aircraft were used to calculate NO_2 and O_x' fluxes from source areas along the flight track.

The advantages to co-deployment of these three remote sensing instruments on a mobile platform for this kind of study are as follows:

1. The flux calculations are fully experimentally constrained. In particular, measurements of wind and BLH along the flight track decouple horizontal and vertical transport; column measurements integrate pollutant concentrations over the BLH, and are inherently insensitive to vertical inhomogeneity.
2. Measurements constrain NO_2, O_3, O_x (O_3+NO_2), enabling studies of NO_x emissions and O_x production rates also over NO_x source areas, i.e., under conditions when O_3 concentrations are reduced due to NO emissions (O_3 titration to form NO_2).
3. Colocation of all three sensors on a single platform minimizes error, and makes the flux calculation straightforward by assuring sampling on similar temporal and spatial scales.

The horizontal flux divergence approach presented here for a case study in the Bakersfield area has comparatively small error for the largest box (Box F) and larger error for the

smallest box (Box C). The overall measurement uncertainty in the individual flux measurement is in the order of 10-11%. The potential error due to entrainment, dry deposition and chemical transformation is of a similar magnitude, and can in the future be further reduced through coupling with atmospheric models. Our measured NO_2 and O_x' production rates reveal higher O_3 production upwind of Bakersfield in an area with active oil and natural gas production. This finding is highly significant within experimental error, and spatially well separated from urban source areas. Comparison of NO_x emissions with the CARB 2010 emission inventory suggest that the NO_x emissions from the urban area are well represented in the inventory. However, the location and timing of the NO_x emissions within the urban area could be improved. In contrast, NO_x emissions over areas with active oil and natural gas production were found to be significantly underestimated; higher background emissions compensate for these local effects over the entire study area. The atmospheric impacts of emissions from oil and natural gas production deserve further investigation.

Models that predict O_3 formation have not previously been constrained by observations at the scale of cities and immediately downwind of cities. The synergistic benefit of combining active and passive remote sensing instruments demonstrated here holds great potential as an innovative tool to improve NO_x emission inventories (emitted amounts and location) as well as constrain O_x production rates experimentally, and over extended areas. The local variations in BLH deserve further investigation as to their role in the exchange of air between the BL and the FT. Further, other trace gases (e.g., formaldehyde and glyoxal) can be measured by AMAX-DOAS and hold largely unexplored potential to extend this approach to the study of VOC oxidation rates. The co-deployment of AMAX-DOAS, TOPAZ lidar and Doppler wind lidar during 51 remaining flights provide a valuable dataset to locate and constrain NO_x emissions over much of California especially the South Coast Air Basin, the Bay area, as well to assess the transport of NO_2 and O_x across the US-Mexican border.

ACKNOWLEDGEMENTS

The authors thank Stuart McKeen (NOAA ESRL, Boulder) for providing the CARB 2010 emission inventory data and the NOAA Twin Otter pilots and flight crew for their support during the campaigns. F.D. acknowledges Halo-Photonics for their help in re-configuring the NCAS Doppler lidar. The scanner for the Doppler lidar was developed with support from CIRES IRP grant to R.M.H. S.B. is recipient of a ESRL/CIRES graduate fellowship. R.V. acknowledges financial support from the California Air Resources Board contract 09-317.

COMPETING INTERESTS

The authors declare no competing interests.

REFERENCES

1. World Health Organisation: Air Quality and Health. 2011; Available at: http://www.who.int/mediacentre/factsheets/fs313/en/. Accessed 09/25, 2013.
2. U.S. Environmental Protection Agency: National Ambient Air Quality Standard (NAAQS). 2012; Available at: http://www.epa.gov/air/criteria.html. Accessed 09/25, 2013.
3. European Commission: Air Quality Standards. 2013; Available at: http://ec.europa.eu/environment/air/quality/standards.htm. Accessed 09/25, 2013.

4. IPCC, 2007: Summary for Policymakers. In: Climate Change 2007: The Physical Science Basis. Contribution of Working Group I to the Fourth Assessment Report of the Intergovernmental Panel on Climate Change [Solomon, S., Qin, D., Manning, M., Chen, Z., Marquis, M., Averyt, K.B., Tignor, M., and Miller, H.L.(eds.)]. Cambridge, United Kingdom and New York, NY, USA: Cambridge University Press.
5. Haagensmit AJ. Chemistry and Physiology of Los-Angeles Smog. Ind. Eng. Chem. 1952;44(6):1342-6.
6. Finlayson-Pitts BJ, Pitts Jr JN. Chemistry of the Upper and Lower Atmosphere. San Diego, CA: Academic Press; 2000.
7. Seinfeld JH, Pandis SN. Atmospheric Chemistry and Physics: from air pollution to climate change. 2nd ed. Hoboken, New Jersey: Wiley-Interscience; 2006.
8. Stedman DH. Photochemical Ozone Formation, Simplified. Environ. Chem. 2004;1(2):65-6.
9. Melamed ML, Solomon S, Daniel JS, Langford AO, Portmann RW, Ryerson TB, et al. Measuring reactive nitrogen emissions from point sources using visible spectroscopy from aircraft. J. Environ.Monit. 2003;5:29-34.
10. Ibrahim O, Shaiganfar R, Sinreich R, Stein T, Platt U, Wagner T. Car MAX-DOAS measurements around entire cities: quantification of NOx emissions from the cities of Mannheim and Ludwigshafen (Germany). Atmos. Meas. Tech. 2010;3(3):709-21.
11. Wang S, Zhou B, Wang Z, Yang S, Hao N, Valks P, et al. Remote sensing of NO2 emission from the central urban area of Shanghai (China) using the mobile DOAS technique. J. Geophys. Res. 2012;117:D13305.
12. Beirle S, Boersma KF, Platt U, Lawrence MG, Wagner T. Megacity Emissions and Lifetimes of Nitrogen Oxides Probed from Space. Science. 2011;333(6050):1737-9.
13. Shaiganfar R, Beirle S, Sharma M, Chauhan A, Singh RP, Wagner T. Estimation of NOx emissions from Delhi using Car MAX-DOAS observations and comparison with OMI satellite data. Atmos. Chem. Phys. 2011;11(21):10871-87.
14. Kleinman LI, Daum PH, Imre D, Lee YN, Nunnermacker LJ, Springston SR, et al. Ozone production rate and hydrocarbon reactivity in 5 urban areas: A cause of high ozone concentration in Houston. Geophys.Res.Lett. 2002;29(10):1467.
15. Senff CJ, Alvarez RJ,II, Hardesty RM, Banta RM, Langford AO. Airborne lidar measurements of ozone flux downwind of Houston and Dallas. J. Geophys. Res. 2010;115:D20307.
16. Clapp L, Jenkin M. Analysis of the relationship between ambient levels Of O-3, NO2 and NO as a function of NOx in the UK. Atmos.Environ. 2001;35(36):6391-405.
17. Warneke C, de Gouw JA, Holloway JS, Peischl J, Ryerson TB, Atlas E, et al. Multi year trends in volatile organic compounds in Los Angeles, California: Five decades of decreasing emissions. J. Geophys. Res. 2012;117:D00V17.
18. Kim S.-W., Heckel A, Frost GJ, Richter A, Gleason J, Burrows JP, et al. NO2 columns in the western United States observed from space and simulated by a regional chemistry model and their implications for NOx emissions. J. Geophys. Res. 2009;114:D11301.
19. Langford AO, Brioude J, Cooper OR, Senff CJ, Alvarez RJ, II, Hardesty RM, et al. Stratospheric influence on surface ozone in the Los Angeles area during late spring and early summer of 2010. J. Geophys. Res. 2012;117:D00V06.
20. Langford AO, Senff CJ, Alvarez RJ,II, Banta RM, Hardesty RM. Long-range transport of ozone from the Los Angeles Basin: A case study. Geophys. Res. Lett. 2010;37:L06807.
21. Neuman JA, Trainer M, Aikin KC, Angevine WM, Brioude J, Brown SS, et al. Observations of ozone transport from the free troposphere to the Los Angeles basin. J. Geophys. Res. 2012;117:D00V09.

22. Sillman S. The relation between ozone, NOx and hydrocarbons in urban and polluted rural environments.Atmos.Environ. 1999;33(12):1821-45.
23. Liu SC, Trainer M, Fehsenfeld FC, Parrish DD, Williams EJ, Fahey DW, et al. Ozone Production in the Rural Troposphere and the Implications for Regional and Global Ozone Distributions. J. Geophys. Res. 1987;92(D4):4191-207.
24. Lin X, Trainer M, Liu SC. On the Nonlinearity of the Tropospheric Ozone Production. J. Geophys. Res. 1988;93(D12):15879-88.
25. Kleinman LI, Daum PH, Lee JH, Lee YN, Nunnermacker LJ, Springston SR, et al. Dependence of ozone production on NO and hydrocarbons in the troposphere. Geophys. Res. Lett. 1997;24(18):2299-302.
26. Carter WPL, Lurmann FW. Evaluation of a Detailed Gas-Phase Atmospheric Reaction-Mechanism using Environmental Chamber Data. Atmos. Environ. 1991;25(12):2771-806.
27. Carter WPL. Computer modeling of environmental chamber measurements of maximum incremental reactivities of volatile organic-compounds. Atmos. Environ. 1995;29(18):2513-27.
28. Ren XR, Harder H, Martinez M, Lesher RL, Oliger A, Simpas JB, et al. OH and HO2 chemistry in the urban atmosphere of New York City. Atmos. Environ. 2003;37(26):3639-51.
29. Volkamer R, Sheehy P, Molina LT, Molina MJ. Oxidative capacity of the Mexico City atmosphere - Part 1: A radical source perspective. Atmos. Chem. Phys. 2010;10(14):6969-91.
30. Sheehy PM, Volkamer R, Molina LT, Molina MJ. Oxidative capacity of the Mexico City atmosphere - Part 2: A ROx radical cycling perspective. Atmos. Chem. Phys. 2010;10(14):6993-7008.
31. Cazorla M, Brune WH, Ren X, Lefer B. Direct measurement of ozone production rates in Houston in 2009 and comparison with two estimation methods. Atmos. Chem. Phys. 2012;12(2):1203-12.
32. Pusede SE, Cohen RC. On the observed response of ozone to NOx and VOC reactivity reductions in San Joaquin Valley California 1995-present. Atmos. Chem. Phys. 2012;12(18):8323-39.
33. Richter A, Burrows JP, Nuss H, Granier C, Niemeier U. Increase in tropospheric nitrogen dioxide over China observed from space. Nature. 2005;437(7055):129-32.
34. van der A RJ, Eskes HJ, Boersma KF, van Noije TPC, Van Roozendael M, De Smedt I, et al. Trends, seasonal variability and dominant NOx source derived from a ten year record of NO(2) measured from space. J. Geophys. Res. 2008;113(D4):D04302.
35. Kim S-W, Heckel A, McKeen SA, Frost GJ, Hsie E-Y, Trainer MK, et al. Satellite-observed US power plant NOx emission reductions and their impact on air quality. Geophys. Res. Lett. 2006;33(22):L22812.
36. Konovalov IB, Beekmann M, Burrows JP, Richter A. Satellite measurement based estimates of decadal changes in European nitrogen oxides emissions. Atmos. Chem. Phys. 2008;8(10):2623-41.
37. Russell AR, Valin LC, Bucsela EJ, Wenig MO, Cohen RC. Space-based Constraints on Spatial and Temporal Patterns of NOx Emissions in California, 2005-2008. Environ. Sci. Technol. 2010;44(9):3608-15.
38. Russell AR, Valin LC, Cohen RC. Trends in OMI NO2 observations over the United States: effects of emission control technology and the economic recession. Atmos. Chem. Phys. 2012;12(24):12197-209.
39. Ryerson T, Andrews AE, Angevine WM, Bates TS, Brock CA, Cairns B, et al. The 2010 California research at the Nexus of air quality and climate change (CalNex) field study. J. Geophys. Res. 2013;118:5830-66.

40. Zaveri RA, Shaw WJ, Cziczo DJ, Schmid B, Ferrare RA, Alexander ML, et al. Overview of the 2010 Carbonaceous Aerosols and Radiative Effects Study (CARES). Atmos. Chem. Phys. 2012;12(16):7647-87.
41. Volkamer R, Coburn S, Dix B, Sinreich R. MAX-DOAS observations from ground, ship, and research aircraft: maximizing signal-to-noise to measure 'weak' absorbers. Proc. SPIE. 2009;7462-746203.
42. Baidar S, Oetjen H, Coburn S, Dix B, Ortega I, Sinreich R, et al. The CU Airborne MAX-DOAS instrument: vertical profiling of aerosol extinction and trace gases. Atmos. Meas. Tech. 2013;6(3):719-39.
43. Platt U, Stutz J. Differential Optical Absorption Spectroscopy: Principles and Applications. Heidelberg: Springer Verlag; 2008.
44. Oetjen H, Baidar S, Krotkov NA, Lamsal LN, Lechner M, Volkamer R. Airborne MAX-DOAS measurements over California: Testing the NASA OMI tropospheric NO2 product. J. Geophys. Res. Atmos. 2013;118:7400-13.
45. Alvarez RJ,II, Senff CJ, Langford AO, Weickmann AM, Law DC, Machol JL, et al. Development and Application of a Compact, Tunable, Solid-State Airborne Ozone Lidar System for Boundary Layer Profiling. J. Atmos. Ocean. Technol. 2011;28(10):1258-72.
46. Browell EV, Ismail S, Shipley ST. Ultraviolet Dial Measurements of O-3 Profiles in Regions of Spatially Inhomogeneous Aerosols. Appl. Opt. 1985;24(17):2827-36.
47. Davis KJ, Gamage N, Hagelberg CR, Kiemle C, Lenschow DH, Sullivan PP. An objective method for deriving atmospheric structure from airborne lidar observations. J. Atmos. Ocean. Technol. 2000;17(11):1455-68.
48. Langford AO, Senff CJ, Alvarez RJ, II, Banta RM, Hardesty RM, Parrish DD, et al. Comparison between the TOPAZ Airborne Ozone Lidar and In Situ Measurements during Tex AQS 2006. J. Atmos. Ocean. Technol. 2011;28(10):1243-57.
49. Pearson G, Davies F, Collier C. An analysis of the performance of the UFAM Pulsed Doppler Lidar for observing the boundary layer. J. Atmos. Ocean. Technol. 2009;26(2):240-50.
50. California Department of Conservation: GIS Mapping. 2013; Available at: http://www.conservation.ca.gov/dog/maps/Pages/GISMapping2.aspx. Accessed 09/25, 2013.
51. California Air Resource Board: 2010 CalNex Modeling Inventory. Available at: http://orthus.arb.ca.gov/calnex/data/. Accessed 09/25, 2013.
52. Hauglustaine DA, Granier C, Brasseur GP, Megie G. The Importance of Atmospheric Chemistry in the Calculation of Radiative Forcing on the Climate System. J. Geophys. Res. 1994;99(D1):1173-86.

Peer-review history:
The peer review history for this paper can be accessed here:
http://www.sciencedomain.org/review-history.php?iid=323&id=10&aid=2531